Composition Gradient and Particle Deformed Zone: An Emerging Correlation

ADITYA PRAKASH, TAWQEER NASIR TAK, ARIJIT LODH, NIRAJ NAYAN,
S.V.S. NARAYANA MURTY, P.J. GURUPRASAD, and INDRADEV SAMAJDAR

Compressive ductility of the as-cast AA7075 was nearly doubled by hot compression and by appropriate homogenization treatment. The latter dissolved the 2nd phase, and introduced compositional gradients around the 'surviving' precipitates. Direct observations, through split channel die compression, revealed a correlation between particle deformed zone (PDZ: deformed aluminum matrix surrounding coarse 2nd phase particle), the composition gradient and the working temperature. Local misorientation in the PDZ reduced, remarkably, with the introduction of composition gradient and higher working temperature. The generation of PDZ, especially the influence of the composition gradient and the working temperature, was modeled successfully with discrete dislocation dynamics (DDD). More importantly, tailoring the composition gradients around the second phase brought out clear technological possibility of improving the as-cast compressive ductility without sacrificing the particle content and the compressive strength.

https://doi.org/10.1007/s11661-018-5076-3

I. INTRODUCTION

AEROSPACE grade AA 7075, a high-strength aluminum alloy, is produced by direct chill (DC) casting.[1–4] However, the cast alloy typically has 2nd phase and micro-porosity.[1–7] These, and even the thermal residual stresses,[8–11] may differ significantly with the casting condition and location. And they may lead to significant degradation in mechanical properties, especially ductility. More specifically, porosity and micro-cracks at the matrix-2nd phase interface may provide an easy path for crack propagation[6,12] and are often attributed to ingot hot cracking.[8,13]

Mitigation typically involves homogenization, or dissolution of the 2nd phase, and extensive hot working to eliminate micro-porosity.[1,5] Interestingly, even the as-cast specimens show significant improvement in ductility at elevated temperature.[8,14] It is thus apparent that the dislocation–precipitate interaction plays a critical role in the ductility of the 7XXX series.

Dislocation–precipitate interaction has a reservoir of rich scientific literature.[15–23] Even in the early 1950s, it was recognized that 'dislocations from activated Frank-Read sources to form closed loops around the particles.'[15] There are excellent articles on strengthening through ordered[24] particles and precipitates with coherency[25] field. More relevant to this manuscript, Ashby[26] had shown that a strain incompatibility exists between the matrix and non-shearable second phase. This is accommodated by the generation of geometrically necessary dislocations (GNDs). For the so-called weak interfaces, the strain incompatibility may also lead to the formation of micro-voids (and pre-mature failure) at the interface.

A series of classical research articles, particularly from Humphreys and co-workers,[27–29] clearly established that large non-shearable 2nd phase precipitates would produce particle deformed zone (PDZ) around them. The existence of PDZ especially becomes relevant with considerations of particle stimulated nucleation during subsequent recrystallization,[27] and the fact that PDZ may trigger extensive strain localizations.[28] Though it is apparent that the formation of the PDZ would depend on the deformation condition, and the existence of 2nd phase plus PDZ may significantly affect the mechanical behavior:[27,29] there are several unknowns. Lattice rotations around the 2nd phase are expected or

---

ADITYA PRAKASH and INDRADEV SAMAJDAR are with the Department of Metallurgical Engineering and Materials Science, Indian Institute of Technology Bombay, Mumbai 400076, India, Contact mail: indra@iitb.ac.in TAWQEER NASIR TAK and P.J. GURUPRASAD are with the Department of Aerospace Engineering, Indian Institute of Technology Bombay, Mumbai 400076, India. ARIJIT LODH is with the IITB-Monash Research Academy, Indian Institute of Technology Bombay, Mumbai 400076, India. NIRAJ NAYAN is with the Department of Metallurgical Engineering and Materials Science, Indian Institute of Technology Bombay and also with the Vikram Sarabhai Space Centre, Trivandrum 695 022, India. S.V.S. NARAYANA MURTY is with the Vikram Sarabhai Space Centre.

Manuscript submitted September 23, 2018.

stipulated to have gradients[30] and even certain crystallographic biases.[31] However, these were never addressed experimentally. More specific to this manuscript, 2nd phase precipitates may develop composition gradients during the heat treatment.[32] However, published literature has not tried to address the possible role of composition gradient on the PDZ, and that has been the focus of this study.

DC cast AA7075 was subjected to two different homogenization treatments. The treatments reduced the number and size of the 2nd phase precipitates, and also incorporated composition gradients around the 'surviving' precipitates. Split channel die plane strain compression (SCDPSC)[33–35] was then used, with different temperatures and strain, to provide direct observations on the PDZ. Further, discrete dislocation dynamic simulations were conducted to capture the trends in experimental observations and the basis of particle–dislocation interactions: an emerging correlation between composition gradient and PDZ. Finally, controlled heat treatment, without significant dissolution of the 2nd phase, was used to establish the possibility of ductility improvements without sacrificing the compressive strength.

II. EXPERIMENTAL PROCEDURE

A commercial Al-Zn-Mg-Cu alloy (chemical composition listed in Table I) was selected for this study. The alloy was manufactured by DC (direct chill) casting of 380-mm diameter ingot. Compression specimens, 8 mm diameter and 12 mm length (along the casting direction), were machined from the center of the ingot as per ASTM E9 standard.[36] The as-cast specimens were generalized as AC, while additional homogenization treatments produced H1 (743 K—20 hours) and H2 (763 K—20 hours) specimens, respectively. The selection of the heat treatment temperatures was based on prior[37] studies and DSC (differential scanning calorimetry) measurements on the present AC specimens. Though the DSC data are not included in this manuscript for brevity: they clearly showed dissolution temperatures for the two intermetallic phases as ~ 740 K and ~ 760 K, respectively. All samples were prepared metallographically: finishing with sub-micron colloidal silica polish. It is to be noted that the quality of the surface finish was adequate to obtain excellent Kikuchi patterns from the aluminum matrix.

Characterization of the second phase involved scanning electron microscope (SEM) backscattered electron (BSE) imaging and also imaging with X-ray microscopy (XRM). For the former, a FEI™ Nova Nano SEM (with energy selective BSE detector: CBS™) was used. ~ 0.3-μm-thick specimens were subjected to XRM, Zeiss™ Xradia 520 Versa, imaging with ~ 0.5 μm voxel resolution. Standard image analysis (ImageJ™) was used for the SEM images, while commercial software (ORS Visual SI™) provided the analysis of XRM data. For identifying the chemistry and crystal structure of the second phase(s), a combination of WDS (wave length dispersive X-ray spectroscopy) and micro-focused XRD (X-ray diffraction) were used. The WDS (from EDAX™) was part of a FEI™ Quanta-3d SEM, while Brukers™ D8-Discover (with micro-focus (~ 50 μm spot size) X-ray, video-laser tracker, and a Vantec™ area detector) was used for crystal structure identification.

Table I. Chemical Composition (in Weight Percent Alloying Elements) of the Alloy (AA7075) Used in This Study

Mn	Si	Cr	Cu	Ti	Zn	Fe	Mg
0.15	0.21	0.24	1.25	0.04	5.2	0.21	2.35

Standard compression tests, at both room and elevated temperatures, were conducted on a Gleeble™ 3800 thermo-mechanical simulator. Compressive ductility values were determined by a sudden drop in true stress. Multiple tests were performed to confirm the reproducibility. The simulator allowed fast (~ 20 K/s) heating and cooling, and a constant strain rate of 0.1 second^{-1}. The same simulator was also used to run split channel die plane strain compression (SCDPSC) test . Such tests involved appropriate Teflon wrapping and graphite lubrication.[33–35] SCDPSC tests enabled direct EBSD (electron backscattered diffraction: TSL™ system) measurements of identical locations at different stages (different strains and temperatures) of plastic deformation.

III. RESULTS

Figure 1 collates the results from the compression tests. More specifically, and as shown in Figure 1(a), compressive ductility improved significantly with the homogenization treatments: from ~ 28 Pct in the as-cast (AC) to ~ 39 Pct and ~ 62 Pct after the H1 and H2 homogenization, respectively. However, the improvement in ductility was accompanied by a drop in strength (Table II(a)). These effects were primarily caused by the dissolution of the 2nd phase (as confirmed later in this manuscript). It is to be noted that particle deformed zone (PDZ: deformed aluminum matrix around the 2nd phase) may form, depending on the deformation condition, around coarse 2nd phase.[11–13] PDZ may trigger strain localizations and hence control the strength, failure, and the ductility.[12] The elevated temperature compression tests, see Figure 1(b) and Table II(b), noticeably improved the ductility (albeit with reduced strength) of the as-cast (AC) specimens. More specifically, ~ 28 Pct ductility (488 MPa saturation strength) in the room temperature tests was enhanced to > 78 Pct ductility (but only 70 MPa strength) after 723 K test. Not only the compression tests were extremely reproducible (as shown in Figure 1(a)), the fast heating and minimal holding of the AC specimens enabled elevated temperature compression tests under an identical presence of the 2nd phase particles. All these results thus provide an interesting, albeit expected,[38,39] technological paradox: any strengthening through coarse non-shearable 2nd phase typically leads to a loss of

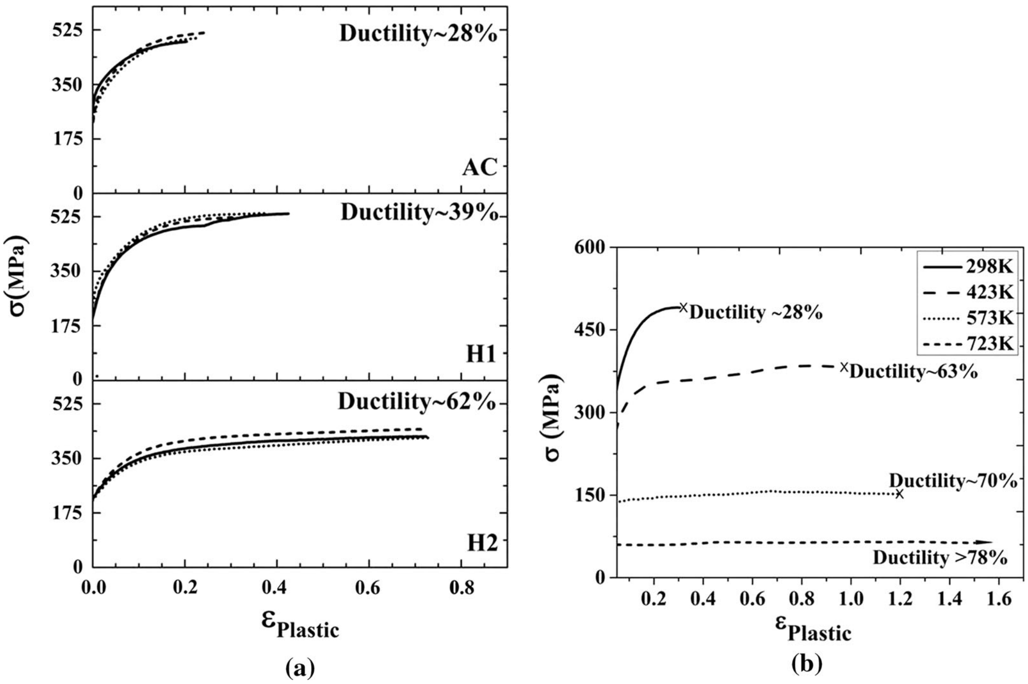

Fig. 1—True stress (σ) *vs* true plastic strain ($\varepsilon_{Plastic}$) for compression tests at (*a*) 298 K and (*b*) 298 to 723 K. In (a) data include both as-cast (AC) and homogenized (H1 and H2) specimens, while (b) shows temperature-dependent compression behavior of the AC specimens. In (a), multiple plots are included to show reproducibility of the tests. Percentage (Pct) compressive ductility values are also mentioned in both figures.

Table II. Compressive Strength and Ductility (Percent Compressive Ductility) Values for (a) 298 K Compression Tests in As-Cast (AC), Homogenized (H2) and Heat-Treated Specimens. (b) Values from 298 K to 723 K Compression Tests in AC. In (a), H2 Involved Significant Dissolution of 2nd Phase (Fig. 3)—While Heat-Treated Specimen (Fig. 8) Had Similar 2nd Phase Content as the AC

Condition	Compressive Strength (MPa)	Ductility (Percent)
(a)		
AC	520	28
H2	378	62
Heat Treated	480	52
(b)		
298 K	520	28
423 K	384	63
573 K	153	70
723 K	70	> 78

ductility. Later in this manuscript, an alternative, improving ductility without sacrificing the strength and the 2nd phase content, is sought by controlling the composition gradients around the coarse 2nd phase.

As the mechanical behavior of a particle containing aluminum alloy is expected to depend on the dislocation 2nd phase interaction,[11,12] identifying the 2nd phase was considered essential. 2nd phase and porosities were identified with both scanning electron microscopy (SEM) and X-ray microscopy (XRM) imaging. This is shown in Figure 2. Under backscattered imaging, the 2nd phase had two different contrasts: black and white. A combination of wavelength dispersive X-ray spectroscopy (WDS) and micro-focus X-ray diffraction (XRD) was used to characterize the 2nd phase. WDS determined the exact chemical composition, while micro-focus XRD from several 2nd phase particles were collated (through an area detector) and then analyzed to identify the crystal structures. These were characterized (see Figure 2) as Al_2CuMg (space group Cmcm) and $Al_2Mg_3Zn_3$ (space group Im3), respectively.

As shown in Figure 3(a), respective homogenization treatments led to a clear reduction in the relative presence of the 2nd phase. The data, from the microstructures, are further collated in Figure 3(b). The figure shows an almost similar drop in both Al_2CuMg and $Al_2Mg_3Zn_3$ with the first homogenization treatment (H1). The final homogenization treatment (H2), however, primarily reduced the area fraction of $Al_2Mg_3Zn_3$. It is clear from these measurements, and earlier studies,[37] that the homogenization led to the dissolution of 2nd phase: their reduced area fraction (by ~ 4 times) and size. A secondary effect of the homogenization treatment was development in the composition gradient. This is shown in Figure 4 for $Al_2Mg_3Zn_3$ 2nd phase. It needs to be noted that similar composition gradients were observed around Al_2CuMg particles as well. In summary, homogenization treatment reduced the relative size and presence of the 2nd phase (both Al_2CuMg and $Al_2Mg_3Zn_3$) and developed a composition gradient. It brought in the major focus of this manuscript: a possible correlation between composition gradient and particle deformed zone (PDZ).

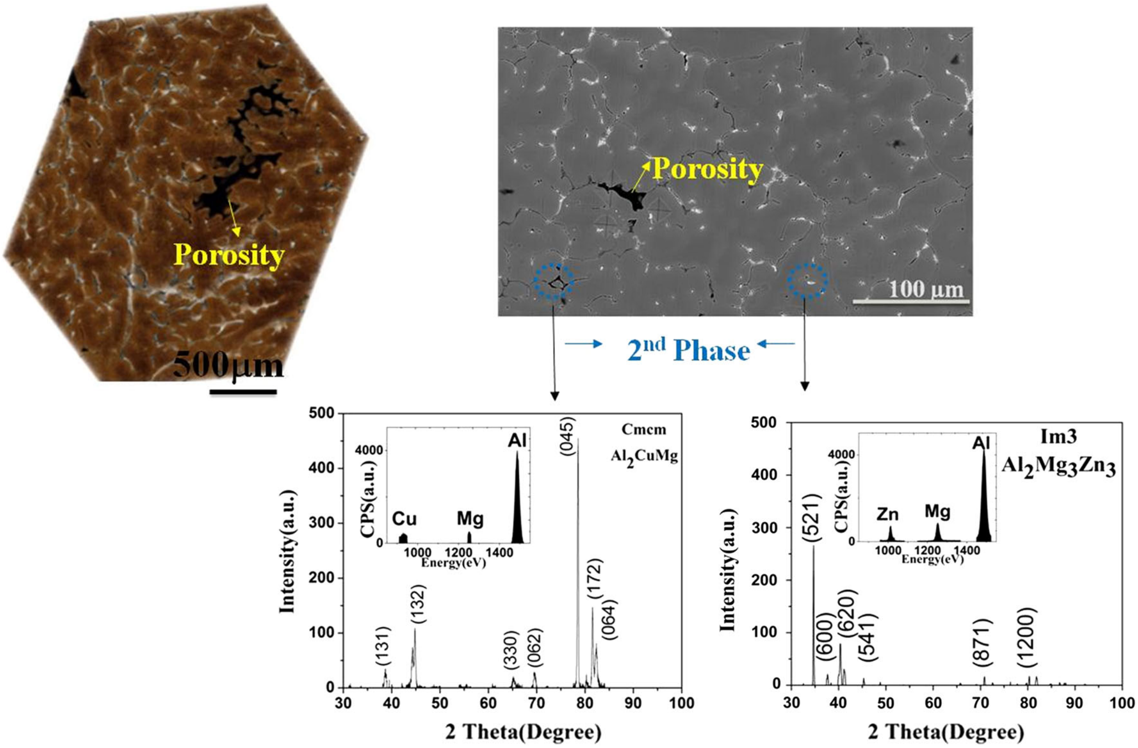

Fig. 2—Images from scanning electron microscopy (SEM) and X-ray microscopy (XRM) showing the presence of 2nd phase and porosity. The former appeared black and white, respectively, under backscattered imaging in SEM. Micro-focused X-ray diffraction and wavelength dispersive spectroscopy (WDS) identified the 2nd phases as Al_2CuMg (space group CmCm) and $Al_2Mg_3Zn_3$ (space group Im3), respectively.

Direct observations on particle deformed zone (PDZ) were made using SCDPSC (split channel die plane strain compression) specimens. As in Figure 5(a), relatively coarse (0.3 μm step size) EBSD scans were able to capture the overall microstructural evolution. However, for the exact quantification of the PDZ: higher resolution (50 nm step size) scans were essential. As shown in Figure 5(b), such scans brought out clear differences in the severity of the PDZ between AC and H2 specimens. To quantitatively represent these observations, two steps were taken. (i) High-resolution EBSD measurements were taken, for each condition, from at least 25 2nd phase particles. The particle size, for such measurements, was kept within 15 to 20 μm. (ii) Kernel average misorientation (KAM) values were then measured within 1.5 times the diameter of the 2nd phase. It is to be noted that the KAM represents average misorientation between each measurement point and all its immediate neighbors (six—as in case of the hexagonal grid used in the present study).

The collated data of the KAM, around the PDZs, brought out some very interesting information. As in Figure 5(c), it quantitatively established that AC (or the 2nd phase without composition gradient) had more KAM than the H2 (2nd phase with composition gradient): a difference that got enhanced with progressive plastic deformation. However, KAM in the AC-PDZ reduced remarkably at the higher deformation temperatures, see Figure 5(d). Figure 5 thus related the relative presence of the PDZ with the composition gradient around the 2nd phase and the imposed deformation temperature. In the next section, in the discussion, an effort has been made to explain these experimental observations in terms of discrete dislocation dynamics (DDD).

IV. DISCUSSION

The DDD simulations were conducted approximating 2nd phase with (as in the case of the homogenized specimen) and without (as-cast specimen) composition gradient. For the as-cast specimen or specimen without a composition gradient, the simulations were also performed approximating different working temperatures. Details of the simulation procedure are given in the Appendix and Table III, while Figures 6 and 7 summarize the simulation output. As shown in Figure 6(a), the non-shearable 2nd phase (and the imposed discontinuity in the slip systems) led to dislocation pile-ups. Qualitatively, the pile-up or geometrically necessary dislocation (GND) density appeared less in simulations with composition or dislocation drag (B—see Appendix) gradient: the so-called homogenized specimen. More specifically, the pinned dislocation density around the 2nd phase evolved with strain, see Figure 6(b) but was a clear function of the composition gradient. When the working temperature was changed, the dislocation glide velocity was suitably altered, see appendix for details. And the DDD simulations showed, qualitatively, GND density around the 2nd phase reduced (Figure 7(a)) at higher working temperatures.

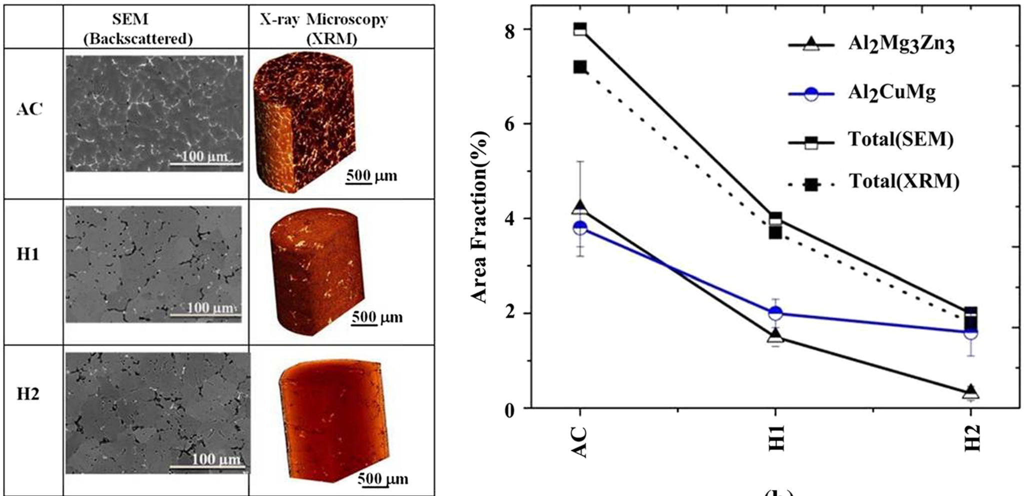

(a)

(b)

Fig. 3—(*a*) Typical microstructures of the as-cast (AC) and homogenized (H1 and H2) specimens, as obtained by SEM and XRM. (*b*) Area fraction of 2nd phase in AC, H1 and H2 specimens. This is shown for both $Al_2Mg_3Zn_3$ and Al_2CuMg (as obtained by SEM imaging), and combined (SEM and XRM data) area fractions.

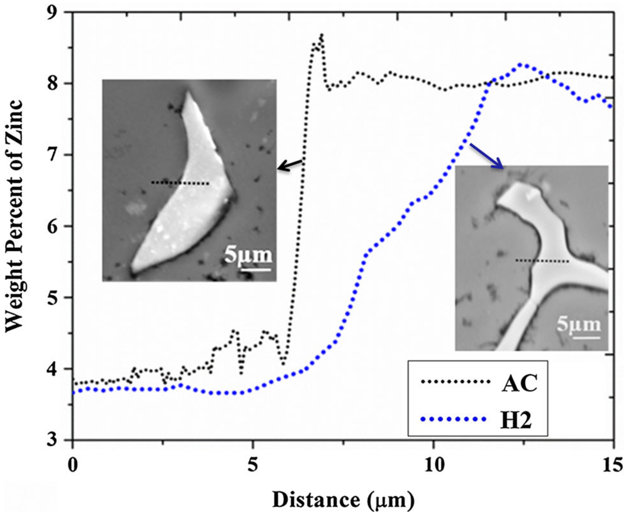

Fig. 4—Typical WDS line scan showing composition gradient around $Al_2Mg_3Zn_3$ 2nd phase in the AC and H2 state. Insets show appropriate SEM images of the 2nd phase.

This is also shown quantitatively in Figure 7(b). In a word, the DDD simulations (Figures 6 and 7: considering only dislocation glide) could capture the important features of the experimental PDZ (Figure 5): (i) PDZ had more misorientation (or GND and pinned dislocation density) without composition gradient and (ii) the misorientation or GND (or pinned dislocation density) reduced with increase in working temperature.

Ashby[26] appears to be the first to propose a model for work hardening in dispersion hardened single crystals. The model explained, qualitatively, the formation of PDZ and captured the patterns of experimental stress–strain behavior. There are excellent follow-ups on the PDZ formation.[27–29] Many of these studies,[28,29] including Ashby's original manuscript,[29] indicate the importance of the particle–matrix interface. The strength of the interface, or possible fracture at the particle–matrix interface, would naturally decide the ductility. This brings a technological dilemma and a practical problem. In a dispersion strengthened alloy, such as the present AA7075, any increase in the strength comes at the cost of ductility.[38,39] Also in large aerospace forgings, it is possible to have a remnant of the cast structure.[40] A homogenization treatment may improve the compressive ductility, but that would also come at a cost of strength.

Based on the direct experimental observations (Figure 5) as well as the numerical simulations (Figure 6), it was felt that a suitable heat treatment (below the 2nd phase dissolution temperature: ~ 763 K for AA7075) may produce composition gradients around the 2nd phase. As shown in Figure 8, such a heat treatment (673 K—50 hours) had identical 2nd phase content, a nominal drop (~ 50 MPa) in strength, but a significant improvement in compressive ductility: ~ 28 Pct in the as-cast specimen to ~ 52 Pct in the heat-treated state. The study thus indicated a possible technological mitigation for the low-ductility regions (or remnant cast structures) in large aerospace forgings. More importantly, it reaffirms the role of precipitate–matrix interface and a suitable composition gradient in improving the fracture performance of a dispersion hardened alloy system. It is important to note that heat treatments (both homogenization to reduce 2nd phase content or heat treatments to introduce compositional gradients around the 2nd phase) are only effective in improving the compressive ductility of the as-cast structures. Any improvements in the tensile ductility demand the elimination of the micro-porosities through extensive hot working. This latter topic remains beyond the purview of the present manuscript and is expected to be covered in the separate publication.

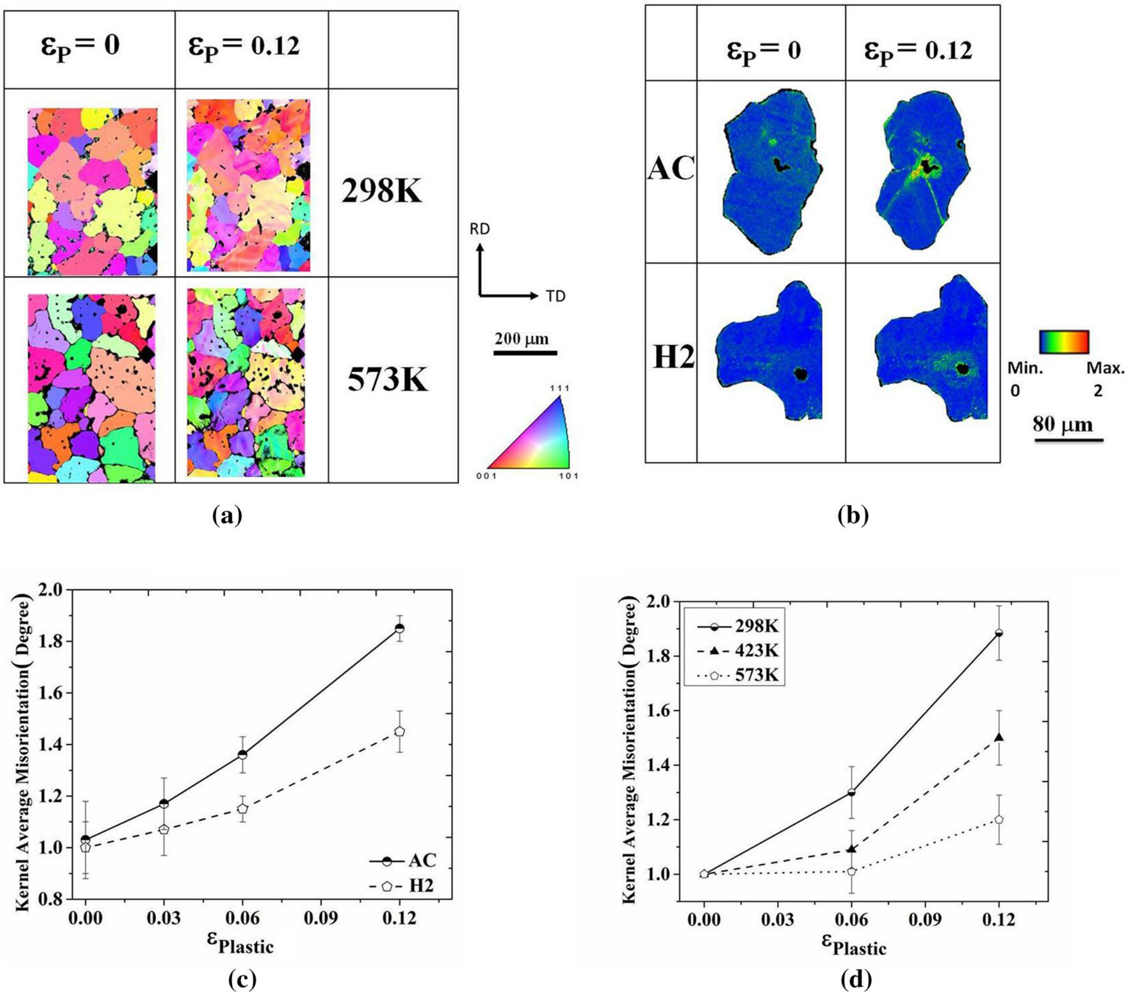

(a)

(b)

(c)

(d)

Fig. 5—EBSD (*a*) inverse pole figure (IPF) and (*b*) kernel average misorientation (KAM) maps. These were taken from AC specimens subjected to SCDPSC (split channel die plane strain compression) at 298 K and 573 K (and a plastic strain, $\varepsilon_{Plastic}$, of 0.12). (a) was taken at a relatively coarse (0.3 μm step size) step, followed by high-resolution (50 nm step size) EBSD around individual 2nd phase particles. Data on particle deformed zone (PDZ), on at least 25 2nd phase particles, were further collated to provide KAM *vs* $\varepsilon_{Plastic}$ for (*c*) AC and H2 specimens after 298 K deformation and (*d*) AC specimens after 298 K to 573 K deformation.

Table III. Parameters Used in the Discrete Dislocation Dynamics Simulations

Elastic Modulus (*E*)	66 GPa
Poisson's Ratio (υ)	0.3
Burgers Vector (*b*)	0.25E−3 μm
Slip Plane Spacing	50b
Drag Coefficient (B_0)	1.0E−4 Pa-s
τ_{FR}	17 MPa
τ_{obs}	150 MPa
α	0.3
β_{bk}	0.5
β_{nu}	1
γ	0.1E4
Time Increment	0.5 ns
Strain Rate	1000 s^{-1}
Schmid Factor	$\{100\}\langle 001\rangle = 0.43$ $\{112\}\langle 111\rangle = 0.40$ $\{011\}\langle 211\rangle = 0.31$

This manuscript was intimated with an objective to explore the PDZ. This is not a new topic and has an exhaustive array of very interesting literature.[11–13,27–29] However, with one notable exception,[41] all experimental studies on PDZ are indirect in nature. The direct observations, see Figure 5, coupled with appropriate numerical simulations clearly have the potential of exploring deformation and fracture behavior, and the associated PDZ formation, in the particle containing alloys.

V. CONCLUSIONS

- Compressive ductility in the as-cast AA7075 was enhanced significantly through homogenization and elevated temperature deformation. Improvements in ductility, in both cases, were accompanied by major reduction in compressive strength.

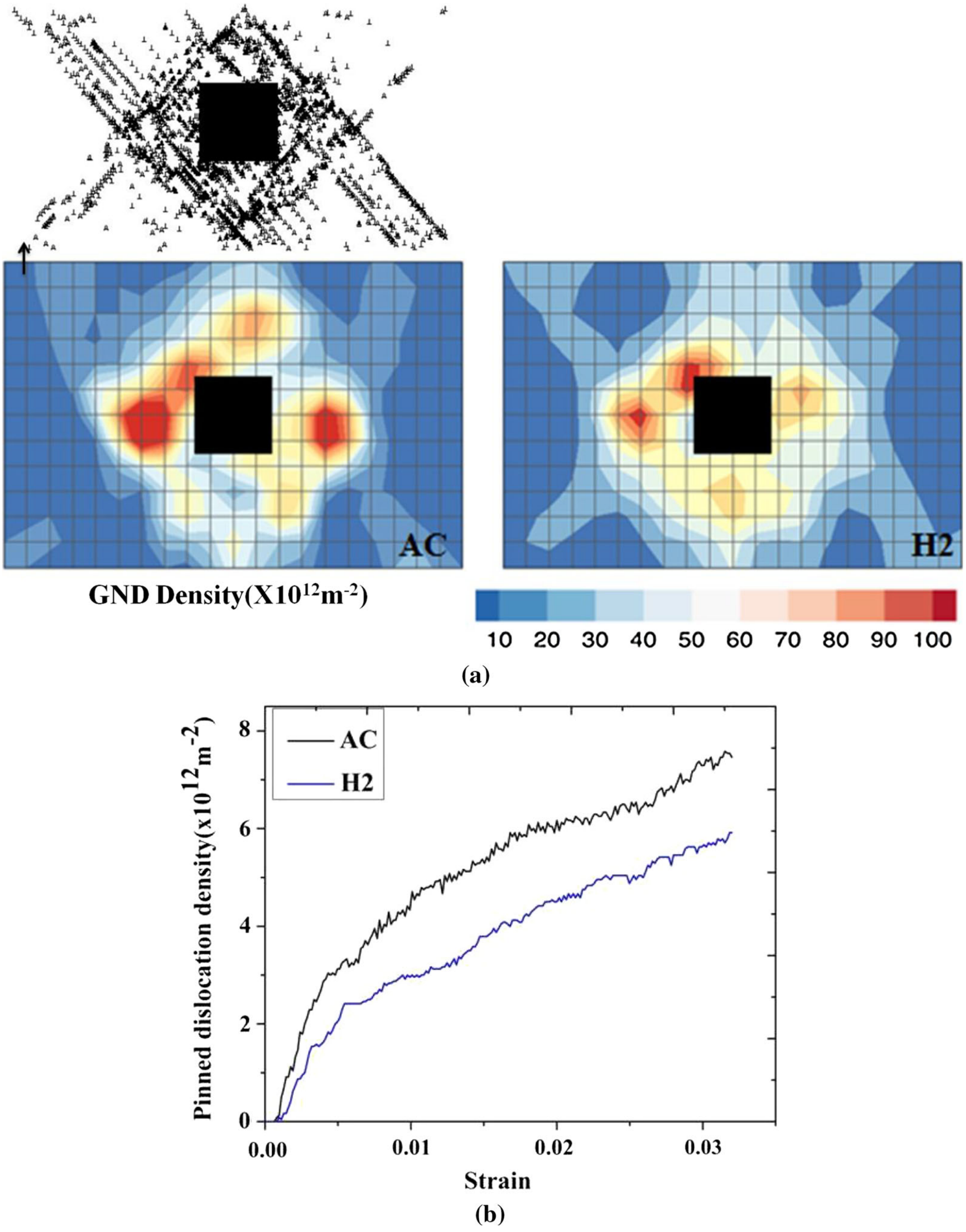

Fig. 6—DDD simulations on the particle deformed zone (PDZ) for the as-cast (AC: 2nd phase without composition gradient) and homogenized (H2: 2nd phase with composition gradient) specimens showing: (*a*) dislocation density contours (drawn from the discrete dislocations present—as shown for the AC) and (*b*) evolution of pinned dislocation density with plastic strain. (a) and (b) thus provide results on simulated PDZ in AC and H2 specimens.

- Homogenization as well as elevated temperature deformation reduced the severity of particle deformed zone (PDZ): deformed aluminum matrix around coarse 2nd phase particles. Homogenization reduced the volume fraction of the 2nd phase (Al_2CuMg and $Al_2Mg_3Zn_3$), but also introduced composition gradients around 'surviving' 2nd phase particles. Direct observation revealed lower misorientation in the PDZ of 2nd phase with composition gradient. Misorientation in the PDZ also reduced with increase in deformation temperature.
- A discrete dislocation dynamics (DDD) model was proposed for 2nd phase with and without composition gradient and for different working temperatures. The simulations captured the patterns of experimental results successfully.
- Based on the experiments and numerical simulations, a heat treatment was proposed to produce

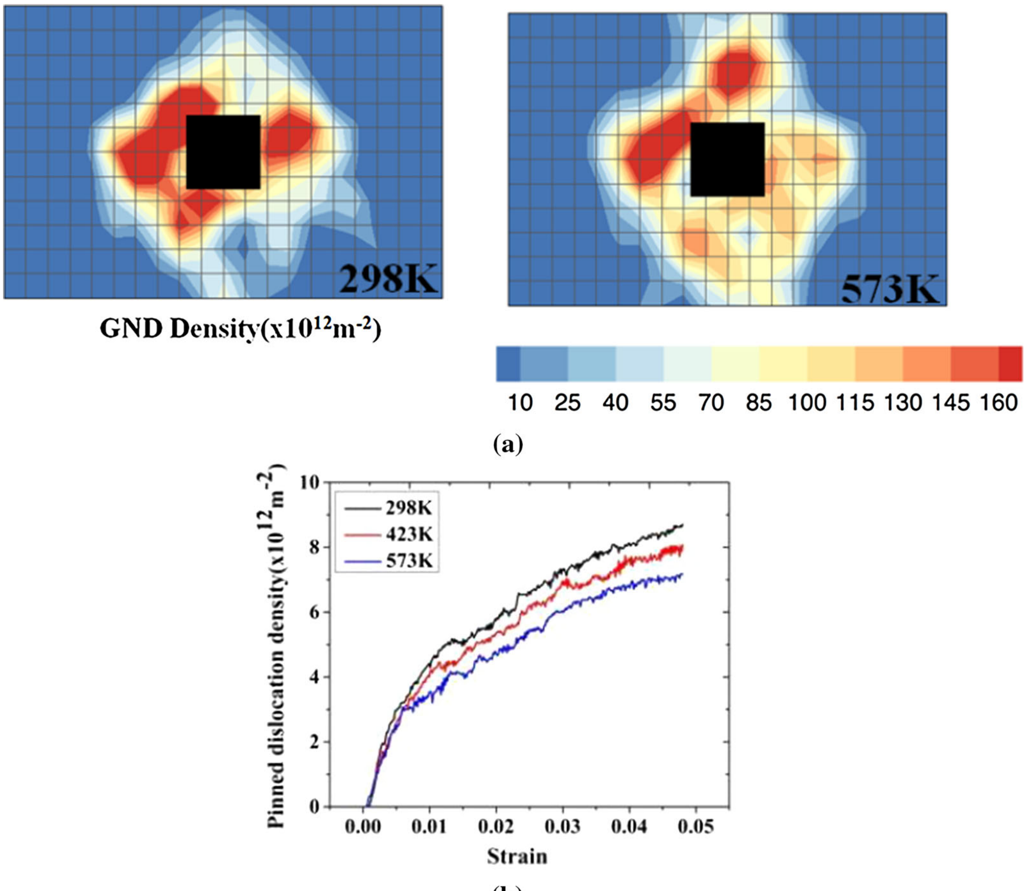

(a)

(b)

Fig. 7—DDD simulations on the particle deformed zone (PDZ) for the as-cast (2nd phase without composition gradient) specimen. (*a*) Dislocation contours showing pinned dislocation and (*b*) evolution of pinned dislocation density with plastic strain. (a) and (b) are shown for different dislocation mobility and corresponding different working temperatures.

composition gradient around the 2nd phase. The treatment provided a clear technological possibility of improving the as-cast compressive ductility without sacrificing the particle content and the compressive strength.

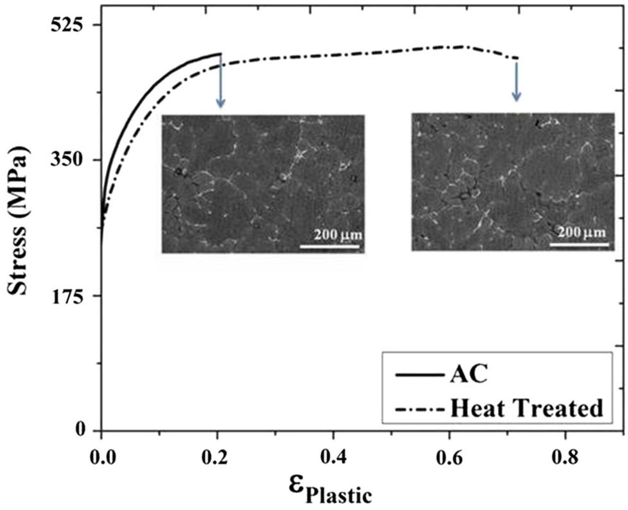

Fig. 8—True plastic stress (σ) *vs* true plastic strain ($\varepsilon_{\text{Plastic}}$) for compression tests at 298 K. These tests were performed on the as-cast (AC) and heat-treated (673 K—50 hours) specimens. Also included are the SEM microstructures of the respective specimens. The later shows almost identical 2nd phase content for both AC and heat-treated specimens.

ACKNOWLEDGMENTS

The authors would like to acknowledge ISRO (Indian Space Research Organisation, India) for support. Support from the National Facility of Texture and OIM, CoEST (thermo-mechanical deformation lab), and 4D X-ray microscope lab are also appreciated.

APPENDIX

The discrete dislocation dynamics (DDD) has been used for studying dislocation–precipitate interaction.[42–44] The formulation, used in this manuscript, follows the framework described by Benzerga *et al.*[45] This formulation accounts for key three-dimensional effects as a set of constitutive rules. In the present model, the framework by Benzerga *et al.*[45] has been extended to account for the effects due to second-phase inclusion in a plastically deformable matrix. Details of the numerical implementation are based on the methodology described in Reference 46.

A schematic of a linear elastic isotropic body containing dislocations distributed within it and a second-phase inclusion is shown in Figure A1. The second-phase inclusion was considered to be elastic. The respective volumes of the linear elastic isotropic body and the second-phase inclusion were Ω and Ω^*. The dislocations were hence distributed in the matrix material with volume $\Omega^{\mathrm{M}} = \Omega \setminus \Omega^*$. The fourth-order elastic tensor of the matrix material and the inclusion were given by C and C^*, respectively. Time-dependent traction boundary conditions were applied on the boundary S_{F}, while the time-dependent displacement boundary conditions were applied on the boundary S_{U}. For this problem, superposition method was used, assuming infinitesimal displacement gradients to determine the state of the body. At any given time increment, the state of the body was defined in terms of displacement, strain, and stress,

$$\boldsymbol{u} = \tilde{\boldsymbol{u}} + \hat{\boldsymbol{u}} \quad \boldsymbol{\epsilon} = \tilde{\boldsymbol{\epsilon}} + \hat{\boldsymbol{\epsilon}} \quad \boldsymbol{\sigma} = \tilde{\boldsymbol{\sigma}} + \hat{\boldsymbol{\sigma}}. \qquad [\mathrm{A1}]$$

The singular (˜) fields were obtained by the superposition of the fields (u^i, ϵ^i, σ^i) associated with individual dislocations,

$$\tilde{\boldsymbol{u}} = \sum_{i=1}^{N} \boldsymbol{u}^i, \quad \tilde{\epsilon} = \sum_{i=1}^{N} \epsilon^i, \quad \tilde{\sigma} = \sum_{i=1}^{N} \sigma^i, \qquad [\mathrm{A2}]$$

where N is the total number of dislocations in the sample. The (˜) fields were the image fields that correct for the actual boundary conditions. The latter were specified in terms of conventional tractions and displacements applied to portions of the boundary S_{U} and S_{F}, respectively. The governing equations and the applied boundary conditions for the problem were mathematically represented as,

$$\nabla \cdot \tilde{\boldsymbol{\sigma}} = 0 \quad \hat{\boldsymbol{\epsilon}} = \nabla \tilde{\boldsymbol{u}} \quad \tilde{\boldsymbol{\sigma}} = C : \tilde{\epsilon} \quad \text{in } \Omega^{\mathrm{M}} \cup \Omega^* \qquad [\mathrm{A3}]$$

with following boundary conditions on $S = S_u \cup S_f$

$$n \cdot \tilde{\boldsymbol{\sigma}} = \tilde{\mathrm{T}} \quad \text{on} \quad S_f \quad \text{and} \qquad [\mathrm{A4}]$$

$$\mathbf{u} = \tilde{\boldsymbol{u}} \quad \text{on} \quad S_u, \qquad [\mathrm{A5}]$$

where n is the outer unit normal to S. The image fields ($\wedge$) corrected for the actual boundary conditions as well as accounted for the presence of inclusion. The governing equations, to obtain the image fields, were,

$$\nabla \cdot \tilde{\boldsymbol{\sigma}} = 0 \quad \hat{\epsilon} = \nabla \tilde{\boldsymbol{u}} \quad \text{in } \Omega^{\mathrm{M}} \cup \Omega^* \qquad [\mathrm{A6}]$$

$$\tilde{\boldsymbol{\sigma}} = \mathrm{C}{:}\hat{\boldsymbol{\epsilon}} \quad \text{in } \Omega^{\mathrm{M}} \qquad [\mathrm{A7}]$$

$$\tilde{\boldsymbol{\sigma}} = \mathbf{C}^* : \hat{\epsilon} + (\mathbf{C}^* - \mathbf{C}) : \tilde{\boldsymbol{\epsilon}} \qquad [\mathrm{A8}]$$

and the associated boundary conditions were

$$\mathbf{n} \cdot \tilde{\boldsymbol{\sigma}} = \tilde{\mathbf{T}} = \mathbf{T}_0 - \tilde{\mathbf{T}} \quad \text{on } S_{\mathrm{f}} \qquad [\mathrm{A9}]$$

$$\boldsymbol{u} = \hat{\boldsymbol{u}} = \boldsymbol{u}_0 - \tilde{\boldsymbol{u}} \quad \text{on } S_{\mathrm{u}}. \qquad [\mathrm{A10}]$$

It is important to notice the contribution of polarization stress to the image fields in the inclusion, which resulted due to the dislocation strain fields and the difference in the elastic properties between matrix and inclusion. The polarization stress ($\hat{\mathrm{p}}$),

$$\hat{\mathrm{p}}_{\mathrm{ij}} = \left(\frac{\mu^*}{\mu} - 1\right)\tilde{\sigma}_{\mathrm{ij}} + \frac{1}{3}\left(\frac{\mu^* B - \mu B^*}{B\mu}\right)\tilde{\sigma}_{\mathrm{ij}}, \qquad [\mathrm{A11}]$$

where, μ and B are used to denote the shear and bulk moduli of the matrix material: μ^* and B^* representing those of the inclusion. The displacement fields due to the presence of dislocations in the matrix were assumed to remain smooth across the interface, which made the problem a well-posed one and could be solved by using Finite Element Method.

For any dislocation configuration to be stable in a deformed body, it has to fulfill the conditions for thermodynamic equilibrium. The dislocations naturally reorganize themselves to minimize the energy of the

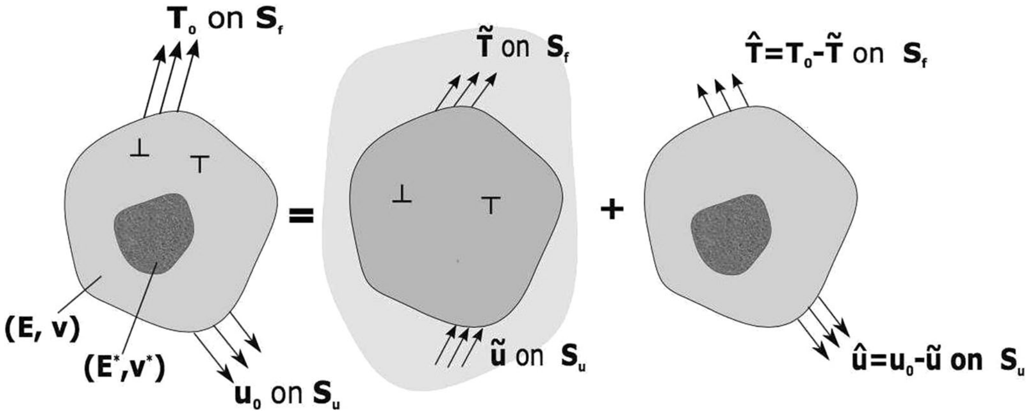

Fig. A1—Describing the model: a body with dislocations and an inclusion. This is further expanded into a problem of interacting dislocations in the infinite solid and a complementary field for the non-homogenous body without dislocations.

system. This rearrangement takes place under the action of a gliding force, referred to as Peach–Koehler force, which essentially can be described as the change of the potential energy of the body associated with an infinitesimal variation of the dislocation position in the glide plane. The expression for the Peach–Koehler force,

$$f^i = \mathbf{m}^i \cdot \left\{ \widehat{\sigma} + \sum_{j \neq i} \sigma^j \right\} \cdot \boldsymbol{b}^i. \qquad [A12]$$

Peach–Koehler force is the primary driving force behind the dislocation glide. The drag-controlled dislocation glide is represented through the following constitutive rule,

$$Bv^i = \mathrm{sign}\left(\boldsymbol{\tau}^i + \zeta^i\right) < \left|\boldsymbol{\tau}^i + \zeta^i\right| - \boldsymbol{\tau}_p > b^i \qquad [A13]$$

with B the viscous drag factor, v^i the glide velocity of dislocation i, $\tau^i = f^i/b^i$, L^i the line tension, and τ_P the Peierls stress. The symbol <·> denotes McCauley's brackets.

Direct experimental observations, see Figure 5, showed the development of particle deformed zone (PDZ). The PDZ was more severe, in terms of local misorientation development, in the as-cast material (2nd phase without compositional gradient) and at lower working temperature. In this manuscript, it was assumed that the compositional gradients affected the viscous drag factor (B). B was hence considered as a function of × (distance from the interface),

$$\mathrm{B}(x) = \mathrm{B}_0 \mathrm{a}^{(1-x)}, \qquad [A14]$$

where $B(x)$ is the drag coefficient at a distance × from the particle–inclusion interface; B_0 is the absolute value of the drag coefficient for the as-cast material at the given temperature. A typical variation of the viscous drag factor B as a function of distance from the matrix–inclusion interface is shown in Figure A2.

Temperature is known to affect dislocation mobility. This can be directly accounted in the framework by considering the viscous drag factor to be a function of temperature, in addition to composition as described above. Groh *et al.*[47] have shown that the viscous drag factor increases with increase in the temperature. In this work, we have followed the relation presented in Reference 47 to obtain viscous drag factor at different temperatures. Since the objective of the simulations is only to qualitatively investigate the effect of composition gradient and temperature on dislocation glide and consequently material deformation behavior, no attempt was made to accurately determine the viscous drag factor through molecular dynamics simulations independently. Further, for the deformation rate controlled simulations considered in this study, climb is not an active dislocation motion mechanism and hence its effect was not considered in the model.

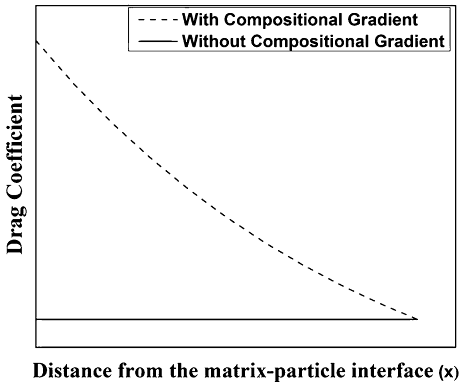

Fig. A2—Schematic showing viscous drag factor (B) *vs* distance particle–matrix interface. These are shown for 2nd phase with and without composition gradient.

REFERENCES

1. D.G. Eskin: *Physical Metallurgy of Direct Chill Casting of Aluminum Alloys*, CRC Press, Boca Raton, 2008.
2. J. Campbell: *Castings: The New Metallurgy of Cast Metals*, 2nd ed., Butterworth-Heinemann Press, Oxford, 2003.
3. J.E. Hatch: *Aluminum Properties and Physical Metallurgy*, 2nd ed., ASM, Aluminium, 1984.
4. J. Grandfield, D.G. Eskin, and I. Bainbridge: *Direct-Chill Casting of Light Alloys: Science and Technology*, The Minerals, Metals & Materials Society, Orlando, 2013.
5. R Nadella, D.G. Eskin, Q. Du, and L Katgerman: *Progr. Mater. Sci.*, 2008, vol. 53, pp. 421–80.
6. M. Lalpoor, D. Eskin, and L. Katgerman: *Mater. Sci. Eng. A*, 2008, vol. 186, pp. 186–94.
7. J.G. Kaufman and E.L. Rooy: *Aluminum Alloy Castings: Properties, Processes, and Applications*, ASM International, Ohio, 2004.
8. M. Lalpoor, D.G. Eskin, and L. Katgerman: *Metall. Mater. Trans. A*, 2000, vol. 40, pp. 3304–13.
9. H.G. Fgaer and A. Mo: *Metall Trans B*, 1990, vol. 21B, pp. 1049–61.
10. J.M. Drezet and M. Rappaz: *Metall. Mater. Trans. A*, 1996, vol. 27, pp. 3214–25.
11. J.M. Drezet and A.B. Phillion: *Metall. Mater. Trans. A*, 2010, vol. 41A, pp. 3396–3404.
12. Q.G. Wang, D. Apelian, and D.A. Lados: *J. Light Metals*, 2001, vol. 1, pp. 73–84.
13. D.G. Eskin, Suyitno, and L. Katgerman: *Progr. Mater. Sci.*, 2004, vol. 49, pp. 629–11.
14. A.G. Luo and M.O. Pekguleryuz: *J. Mater. Sci.*, 1994, vol. 29, pp. 5259–71.
15. J. Fisher, E.W. Hart, and R. Pry: *Acta Metall.*, 1953, vol. 1, pp. 336–39.
16. J.D. Embury and R. Nicholson: *Acta Metall.*, 1963, vol. 11, pp. 347–54.
17. J.T. McGrath and WJ Bratina: *Acta Metall.*, 1967, vol. 15, pp. 329–39.
18. A.J. Ardell: *Metall Trans A*, 1985, vol. 16, pp. 2131–65.
19. U. Messerschmidt and M. Bartsch: *Mater. Sci. Eng: A*, 1993, vol. 164 (1–2), pp. 332–39.
20. B.Q. Li and F.E. Wawner: *Acta Mater.*, 1998, vol. 46, pp. 5483–90.
21. T. Gladman: *Mater. Sci. Technol.*, 1999, vol. 15, pp. 30–36.
22. K.E. Huang, K. Marthinsen, Q. Zhao, and R.E. Logé: *Progr. Mater. Sci.*, 2018, vol. 92, pp. 284–59.
23. A. Takahashi and N.M. Ghoniem: *J. Mech. Phys. Solids*, 2008, vol. 56 (4), pp. 1534–53.
24. R.O. Williams: *Acta Metall.*, 1957, vol. 5, pp. 241–44.
25. J. Douin, P. Donnadieu, and F. Houdellier, *Mater. Sci. Eng. A*, 2001, Vol. 319–321, pp 270–73.
26. M. Ashby: *Philos. Mag.*, 1966, vol. 14, pp. 1157–78.
27. F.J. Humphreys and M. Hatherly: *Recrystallization and Related Annealing Phenomena*, Elsevier, Oxford, 2012.
28. F. Humphreys and P. Kalu: *Acta Metall.*, 1987, vol. 35, pp. 2815–29.
29. F. Humphreys and M.G. Ardakani: *Acta Metall.*, 1994, vol. 42, pp. 749–61.

30. P. Vanhoutte: *Acta Metall.*, 1995, vol. 43, pp. 2859–79.
31. R. Orsund, J. Hjelen, and E. Nes: *Scr. Metall.*, 1989, vol. 23, pp. 1193–98.
32. C. Mondal and A.K. Mukhopadhyay: *Mater. Sci. Eng. A*, 2005, vol. 391, pp. 367–76.
33. S. Panchanadeeswaran, R. Doherty, and R. Becker: *Acta Mater.*, 1996, vol. 44, pp. 1233–62.
34. J. Singh, S. Mahesh, G. Kumar, P. Pant, D. Srivastava, G. Dey, N. Saibaba, and I. Samajdar: *Metall. Mater. Trans. A*, 2015, vol. 46, pp. 5058–71.
35. N. Keskar, S. Mukherjee, K.M. Krishna, D. Srivastava, G. Dey, P. Pant, R. Doherty, and I. Samajdar: *Acta Mater.*, 2014, vol. 69, pp. 265–74.
36. ASTM Standard: *E9 (2009) Standard Test Methods of Compression Testing of Metallic Materials at Room Temperature*, ASTM International, West Conshohocken, PA, 2003.
37. N. Nayan, S.V.S. Murty, Gotving, M.C. Mittal, and P.P. Sinha: *Metal. Sci. Heat Treat.*, 2009, vol. 51, pp. 7–8.
38. B.I. Edelson and W.M. Baldwin: *ASM Trans.*, 1962, vol. 55, pp. 230–50.
39. B. Verlinden, J. Driver, I. Samajdar, and R.D. Doherty: *Thermo-Mechanical Processing of Metallic Materials*, Elsevier, Amsterdam, 2007.
40. S.K. Manwatkar, J. Srinath, S.V.S. Narayana Murty, P. Ramesh Narayanan, S.C. Sharma, and P.V. Venkitakrishnan: *J. Fail. Anal. Preven.*, 2016, vol. 16, pp. 1141–49.
41. P.S. Karamched and A.J. Wilkinson: *Acta Mater.*, 2011, vol. 59, pp. 263–72.
42. C.S. Shin, M.C. Fivel, M. Verdier, and K.H. Oh: *Philos. Mag.*, 2003, vol. 83, pp. 3691–3704.
43. A. Takahashi and N.M. Ghoniem: *J. Mech. Phys. Solids*, 2008, vol. 56, pp. 1534–53.
44. A. Lehtinen, F. Granberg, L. Laurson, and K. Nordlund: *Phys. Rev. E*, 2016, vol. 93 (1–9), p. 013309.
45. A.A. Benzerga, Y. Brechet, A. Needleman, and E. Van der Giessen: *Modell. Simul. Mater. Sci. Eng.*, 2004, vol. 12, pp. 159–96.
46. E. Giessen and Needleman: *Modell. Simul. Mater. Sci. Eng.*, 1995, vol. 3, pp. 689–35.
47. S. Groh, E.B. Marin, M.F. Horstmeyer, and H. Zbib: *Int. J. Plast.*, 2009, vol. 25, pp. 1456–14.